buildings

MDPI

Article

Seismic Response Compression of Various MSE Walls Based on 3D Modeling

Muhammad Akbar [1,2], Huali Pan [1,*], Guoqiang Ou [1], Georgios Nikitas [3] and Bilal Ahmed [4]

[1] Institute of Mountain Hazards and Environment, Chinese Academy of Sciences, Chengdu 610299, China; akbarmohammad0092@gmail.com (M.A.)
[2] University of Chinese Academy of Sciences, Beijing 100049, China
[3] School of Transportation and Civil Engineering, Nantong School of Civil Engineering and Built Environment, Liverpool John Moores University, Liverpool L3 3AF, UK
[4] Department of Structural Engineering, Faculty of Civil Engineering, Doctoral School, Silesian University of Technology, Akademicka 2, 44-100 Gliwice, Poland; bilal.ahmed@polsl.pl
* Correspondence: hlpan@imde.ac.cn

Abstract: This study evaluates the earthquake-induced movement of mechanically stabilized earth (MSE) walls. A thorough investigation was conducted on an MSE wall model, utilizing a comprehensive finite element (FE) analysis. This research focuses on investigating and designing MSE walls made of reinforcement concrete and hollow precast concrete panels. It also involves comparative studies such as on the vertical pressure of the wall, horizontal pressure of the wall, lateral pressure of the wall, settlement of the wall, settlement of the backfill reinforcement, vertical pressure of the backfill, horizontal pressure of the backfill, lateral pressure of the backfill, vertical settlement of the foundation, and settlements of soil layers across the height of the MSE walls. The FE simulations used a three-dimensional (3D) nonlinear dynamic FE model of full-scale MSE walls. The seismic performance of MSE walls has also been examined in terms of wall height. It was found that the seismic motion significantly impacts the height of the walls. In addition, the validity of the proposed study model was assessed by comparing it to the reinforcement concrete wall and ASSHTO guidelines using finite element (FE) simulation results. Based on the findings, the hollow prefabricated MSE wall was the most practical alternative due to its lower displacement and settlement. The specifics of the modeling approach used in this study and the lessons learned serve as benchmarks for future comparable lines of inquiry and practitioners, especially as the computational power of desktop computers continues to rise.

Keywords: seismic analysis; structural resilience; mechanically stabilized earth (MSE); hollow precast concrete walls; nonlinear dynamic; finite element modeling (FEM)

check for updates

Citation: Akbar, M.; Pan, H.; Ou, G.; Nikitas, G.; Ahmed, B. Seismic Response Compression of Various MSE Walls Based on 3D Modeling. *Buildings* **2023**, *13*, 2773. https://doi.org/10.3390/buildings13112773

Academic Editors: Yann Malecot and Asimina Athanatopoulou-Kyriakou

Received: 15 August 2023
Revised: 15 October 2023
Accepted: 19 October 2023
Published: 3 November 2023
Corrected: 21 November 2024

Copyright: © 2023 by the authors. Licensee MDPI, Basel, Switzerland. This article is an open access article distributed under the terms and conditions of the Creative Commons Attribution (CC BY) license (https://creativecommons.org/licenses/by/4.0/).

1. Introduction

A well-known mechanically stabilized earth (MSE) construction method uses discontinuous gradual concrete-facing panels, and geogrid or steel mesh is the most common backfill soil-reinforcement component [1,2]. This paper is focused on geogrid backfill soil-reinforced and hollow precast concrete-facing panels. These structures' seismic response design is often based on nonlinear dynamics methods with empirical adjustments applied to familiar concepts. For MSE walls constructed with continuous facing panels along the running length of backfill facing direction, 3D numerical modeling using the finite element method (FEM) and Abaqus V 614.3 is best suited for this purpose. Numerous researchers have investigated the seismic behavior of MSE walls after earthquakes occurred [3–5]. Significant damage to earth-retaining structures, bridges, and highways close to the epicenter was seen during the 2005 Pakistan earthquake (0.6 g, highest recorded peak ground acceleration, PGA), coupled with excessive sliding and twisting of reinforcement concrete earth-retaining walls (GSP, EERA, [6,7]). The earth-retaining wall experienced significant

sliding and rotation due to the 2019 earthquake, which recorded a maximum peak ground acceleration of 0.4 g (GSP, EERA, [6,7]).

Mechanically stabilized earth (MSE) wall seismic performance and internal stability are often designed using nonlinear dynamics techniques with empirical corrections applied to well-known principles of seismic pressure on structures [8,9]. The lateral pressure of walls, reinforcement settlements, deflection, and displacement are typically evaluated through shaking table experiments and FE simulations across various retaining wall designs [10,11]. The researchers in [12] concluded that the finite element (FE) technique could accurately predict the backfill pressure on retaining walls based on their numerical simulations of different types of retaining walls. The lateral force acting on quay walls is found to be significantly influenced by the lateral seismic coefficient and the height of the wall, as demonstrated in a study [13] that utilized finite element analysis to apply seismic pressure from the wall and simulate the earthquake-induced lateral pressure on quay walls.

The results of an FE study and tests comparing flexible and rigid retaining walls revealed that the flexibility of base-retrained retaining walls substantially affected backfill pressure [14]. A detailed analytical analysis of the seismic performance of rigid retaining walls [15] concentrated on the significance of wall height during experiments. The finite element (FE) method was employed to investigate the passive response of a rigid concrete retaining wall. The study revealed that the size of the failure domain increased with the application of base excitation [16]. The study in [17] determined that a nonlinear distribution of backfill pressure behind a flexible MSE wall could be calibrated using finite element (FE) analysis. To better comprehend the force that dynamic backfill places on the wall and its various failure mechanisms, numerous studies have used shaking tables and FE analysis on miniature MSE wall models [18,19]. They discovered that the backfill soil may significantly impact the seismic performance of MSE-retaining walls. Estimating earthquake-induced displacement of MSE-retaining walls is critical to current performance-based seismic design [20]. Ling HI et al. [21] modified the Newmark sliding block model to forecast earthquake-induced retaining wall movement. Nimbalkar et al. [22] found a nonlinear dynamic soil pressure along the basement wall height and that the typical MO technique yields conservative seismic force estimates when evaluating basement walls numerically.

Finite element analysis was used to investigate the impact of backfill on the seismic response of a mechanically stabilized earth (MSE) wall. The effect of backfill cohesiveness on thrust placement is shown to be minor. The authors embraced the destruction of retaining wall backfill caused by earthquakes [23,24]. The nonlinear FE technique overestimates the displacement of sliding retaining walls caused by earthquakes [25]. A rigorous computational analysis to better understand the earthquake-induced displacement of free-standing MSE walls in near-fault ground excitations discovered large retaining wall displacements [26,27]. The prefabricated wall was eco-friendlier than the concrete MSE wall. According to the research, the prefabricated MSE wall outperformed the reinforcement retaining wall regarding CO_2 emissions, greenhouse impact, essential material cost, and embodied energy [28,29]. The research aimed to establish a technique for conducting a seismic analysis of MSE earth-retaining structures using FE analysis. This was accomplished through a 3D finite element analysis. However, seismic performance is the main topic of a rigorous 3D finite element analysis of hollow prefabricated (MSE) walls. After carefully examining the literature review and to the best of the authors' knowledge, there has not been an extensive probe of prefabricated MSE walls for utilization in highways and infrastructure implementations, either experimentally or employing FE analysis. As a result, there has been no worldwide discovery regarding these prefabricated MSE-retaining wall systems [30].

This research aims to apply nonlinear dynamic finite element analysis to investigate the seismic performance of hollow precast reinforced (MSE) walls. This is the first study to investigate the effects of earthquakes on various forms of hollow precast MSE walls. Using different wall model heights should help researchers and policymakers comprehend the

earthquake-related development impacts in multiple countries. Parallel to this, this study investigates a wide range of variables, including top displacement of the wall, vertical pressure of the wall, horizontal pressure of the wall, lateral pressure of the wall, settlement of the wall, settlement of the mesh, vertical pressure of the backfill, horizontal pressure of the backfill, lateral pressure of the backfill, vertical settlement of the foundation, and stress distribution of the wall. Therefore, the researchers assumed that this objective was attainable. Although the variables' effect on the retaining wall's performance may differ from the seismic force, these groups can maintain their vitality regardless of geographic location. The variables influencing the seismic performance of MSE walls are presented in Table 1.

Table 1. Studies determining the variables influencing the MSE wall under earthquakes.

References	Authors	Country	Type of Wall-Facing	Vertical Pressure	Horizontal Pressure	Lateral Pressure	Settlement of Wall	Settlement of Mesh	Backfill Vertical Pressure	Backfill Horizontal Pressure	Backfill Lateral Pressure	Vertical Foundation Pressure	Displacement of the Wall	Methodology
[5]	I.P. Damians (2020)	Spain	Concrete	×	×	√	×	√	√	√	√	√	×	Numerical simulation
[9]	Bakr J. et al. (2018)	United Kingdom	Concrete	×	√	√	×	×	×	√	×	×	√	Numerical simulation
[29]	J. Vlcek (2014)	United Kingdom	Concrete	×	√	×	×	×	×	×	×	×	√	Numerical simulation
[31]	Tiwari R. et al. (2022)	Australia	Concrete	×	√	×	√	×	×	×	×	×	×	Numerical simulation
[32]	Wang L. et al. (2015)	China	Concrete	×	√	×	√	×	×	×	×	×	×	Physical test and numerical simulation
[33,34]	Yu Y. et al. (2015, 2016)	China	Concrete	×	√	×	×	√	×	×	×	√	√	Numerical simulation
	This research	Pakistan	Precast concrete panel	√	√	√	√	√	√	√	√	√	√	FEA of models with different heights

2. Numerical Modeling Approach

Finite element (FE) analysis was conducted on three-dimensional models of mechanical stabilized earth (MSE) walls to examine their seismic response. A parametric study was carried out to investigate and analyze the seismic response of three distinct wall heights, namely PC-W1 (6 m), PC-W2 (8 m), and CR-W (6 m), in terms of the impacts on two hollow precast concrete MSE walls and one reinforcement concrete MSE wall. The FEA results were utilized in nonlinear dynamic analyses to comprehend the seismic response of the model better. Therefore, the input base accelerations, also known as accelerograms, have been scaled to be 0.3 g times the peak ground acceleration (PGA) [6]. The responses of the MSE walls to vertical pressure of the wall, horizontal pressure of the wall, lateral pressure of the wall, settlement of the wall, settlement of the mesh, vertical pressure of the backfill, horizontal pressure of the backfill, lateral pressure of the backfill, vertical foundation pressure, and settlements of soil layers have all been analyzed based on the results of finite element computations. The numerical modeling showed that the boundary conditions, zone dimensions, and property assignment significantly impact the seismic response behavior of these types of walls; they perform a significant role in the model simulations [5]. The connections between (1) the bottom of the foundation dirt being fixed in both the horizontal and vertical dimensions, (2) the two sides of the foundation soil, and (3) the left side of the retained soil being attached only in the horizontal direction are

studied. Abaqus's acceleration- and displacement-controlled boundary option established the FE model's confines [5,35].

In addition, the presence of geostatic stresses in the backfill and base rock zones has been established. The primary goal of providing a detailed description of the geostatic pressures was to verify the accuracy of the FE analysis and the distribution of the forces [31]. All elements of the finite element mesh were 10-noded hexahedra, including the zones used to simulate the interfaces of dissimilar materials. The finite element mesh had 13,128 elements and 14,888 nodes. In numerical simulations, the lower domain boundary was fixed. The foundation, situated at a depth of 2 m below the wall, was determined to be sufficiently distant to have little impact on numerical results in a practical context. The vertical y–z boundaries were fixed in the cross-plane (x) direction. Hence, the soil and panel y–z boundaries in the vertical (y) direction were free to move. The domain boundaries at the front of the foundation zone and the back of the foundation and retained fill zones were free to move in the vertical direction. The seismic loading was applied to the base of the finite element (FE) model using the acceleration along the x-axis. The vertical mobility of the domain boundaries was uncontrolled in both the front foundation zone and the retained fill zones. Choosing the wall-facing distance from the domain's rear boundary is a pragmatic compromise to reduce the impact of far-field boundaries on wall-facing deformations and runtime. The constraints use the insert option; the base surface is fixed in this context and must not move or rotate in any direction. The numerical analysis included historical earthquake waves and a wall height parameter to analyze the seismic response.

2.1. Material Modeling

This study uses three classes of materials to construct the Abaqus FE model for analysis, as shown in Table 1. The Abaqus [36] wire element feature was utilized to build the reinforcement geogrid, and the CDP model of concrete damaged plasticity was used. The Mohr–Coulomb material (MC) model has been utilized to construct the backfill constitutive behavior. The plane strain conditions have been hypothesized to have contributed to creating the 3D model [28,31]. Additionally, gravitational forces have been included across the entirety of the FE model. The seismic loading was applied to the foundation of the FE model by using the acceleration along the x-axis. Large-deformation numerical analysis sees the widespread application of the nonlinear dynamic explicit solution approach implemented by the FE program Abaqus [36]. An explicit central difference integration rule and many short time steps are used in Abaqus' dynamic explicit analyses to address boundary conditions concerns. The FEA results were taken at a low sample rate to reduce noise in the data [36,37]. The study uses three different MSE walls for simulation: two walls, a hollow precast concrete panel, and a third reinforcement concrete MSE wall. The details of geometry specification are shown in Figures 1 and 2. The hollow precast concrete wall components are shown in Figure 1 the rebar in hollow of the wall sections throughout the foundation improve the wall deformation and deflection behavior; the rebar specification used in this study is shown in Table 2. The wall of each panel has a 1 m length, as shown in Figure 1.

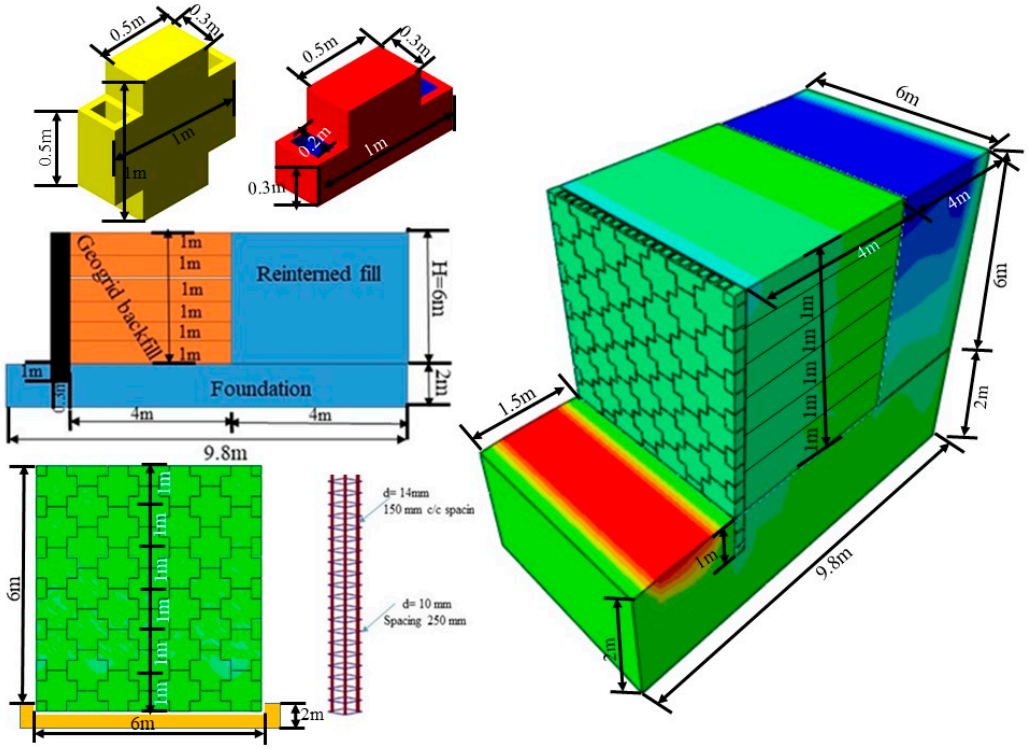


Figure 1. A 3D model overview and precast hollow concrete MSE wall structural components.

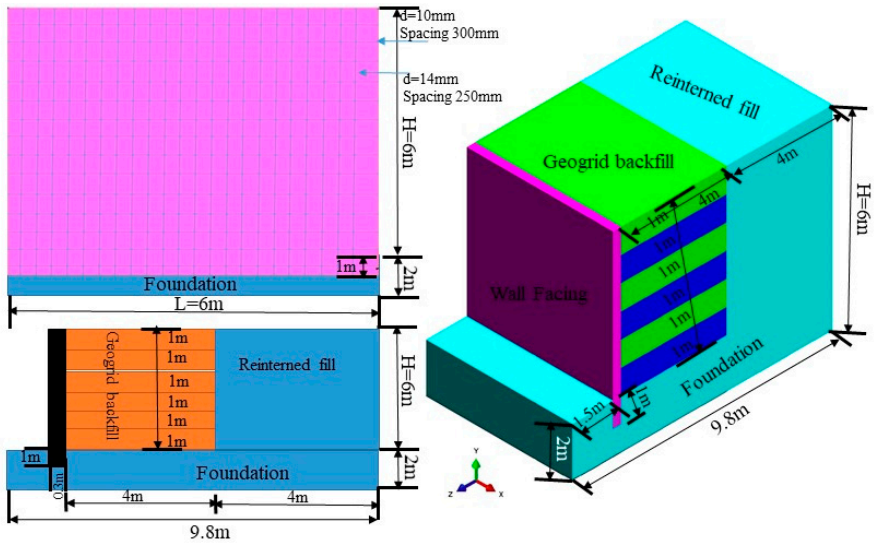


Figure 2. Detailed dimensions of reinforcement concrete MSE wall structural components.

Table 2. MSE Wall Design Considerations.

Parameters	Precast Retaining Wall	Reinforcement Concrete Retaining Wall
	Value (PC-W1, PC-W2)	Value (CR-W)
Wall height (m)	6 m and 8 m	6 m
Backfill soil density (kN/m^3)	18	18
Angle of surcharge (degree)	0°	0°
Angle of repose (degree)	30°	30°
Density of concrete (kN/m^3)	30	30

Table 2. *Cont.*

Parameters	Precast Retaining Wall	Reinforcement Concrete Retaining Wall
	Value (PC-W1, PC-W2)	Value (CR-W)
The safe barring capacity of soil (kN/m^2)	150	150
Friction angle	40°	40°
Compressive strength of concrete (N/mm^2)	30	30
Steel's yield strength (N/mm^2)	415	415
Factor of safety	1.5 to 2.0	1.5 to 2.0
Effective cover (mm)	40	45
Elastic modulus (MPa)	32,000	32,000
Poisson's ratio	0.2	0.2
Model	Concrete damaged plasticity (for concrete)	Von Mises plasticity (for reinforcement)

2.2. Constitutive Modeling of the Backfill and Base Case

A detailed parametric investigation has been carried out for granular backfill types to understand the role of backfill in the overall seismic performance of the MSE wall. The mechanical properties of the backfill materials are shown in Table 3. Using the relationship proposed by [36], the peak friction angle 40° corresponds to 38° from triaxle tests [5]. This value is typical for high-quality granular fill materials recommended in AASHTO [3] specifications for MSE walls. A value of cohesion c = 1 kPa was selected to ensure numerical stability at the soil zone (top) free boundaries during construction [5]. The length of the backfill reinforced zone is about L = 4 m, which is 1 H, where H is the wall height, as shown in Figure 3. The numerical simulations did not include any surcharge at the top boundary of the model. Observing the constitutive behavior of soils during the consolidated-drained (CD) triaxial test [31]. The Mohr–Coulomb (MC) material model was used to simulate the constitutive behavior of granular backfill. Several investigations [38] simulated backfill pre- and post-yield behavior using the MC material model.

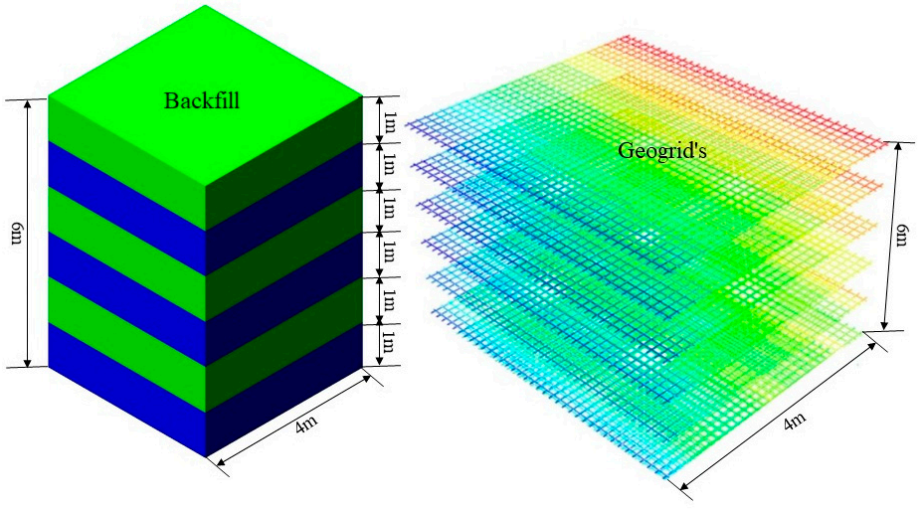


Figure 3. Detailed overview with structural demission of the backfill and geogrid.

It should be noted herein that the post-yield behavior of soil could also be simulated by providing an extension to the MC material model [39,40]. Consequently, the MC model of granular backfills has been applied to the results of the FE investigations in this study. Song [40] has presented details of the MC material model and calibrations using triaxial test results. The triaxial test outcomes, namely the hardening and softening behaviors obtained from the calibrated MC material model, were compared to the laboratory triaxial results of granular backfills. Some authors published the specifics of MC material modeling,

calibrations of the post-yield response of backfill using triaxial test data, and modeling of Rayleigh damping of backfill in an investigation [35]. This study modeled the geogrid mesh used for backfill reinforcing with wire components in Abaqus [36]. Thin reinforcing geogrids are layered into the backfill soil for structural support. It is possible to determine a limit for the geogrid components' tensile failure strain, and these components can give either under tension or under compression. The shear behavior at the geogrid–soil interface is characterized by a nonlinear shear failure wrapping that shifts in shape depending on the confining pressure. The geogrid components' characteristics are shown in Table 4, which provides a summary to replicate the geogrid's primary and secondary reinforcements laid. The arrangement of the geogrid layers was horizontal in the reinforced zone. The geogrid is embedded in the backfill materials, and the geogrid lengths are the same as those of the backfill material. The geogrid soil was constructed with 6 and 8 layers, as shown in Figure 3, where the distance between layers was 1 m.

Table 3. The soil material parameters for the baseline scenario [41].

Parameter	Soil Material (Backfill)	Foundation
Unit weight (kN/m^3)	18	20
Elastic modulus (MPa)	20	35
Poisson's ratio	0.3	0.3
Cohesion (kPa)	1	5
Friction angle (degree)	44°	36°
Dilatancy angle (degree)	14°	6°
Model	Mohr–Coulomb (MC) material model	

Table 4. Properties of backfill geogrid material [42].

Parameters	Geogrid
Calculation width (mm)	1000
Number of meshes per calculation width	1000
Mesh width (mm)	1000
Elastic modulus (MPa)	2700
Mesh thickness (mm)	3
Tensile stiffness (kN/m^2)	6400
Tensile strength (kN/m^2)	416
Interface normal and shear stiffness (kN/m^2)	92,000
Soil interface cohesion (kN/m)	4.0
Model	Von Mises plasticity (for geogrid)

2.3. Concrete and Steel Constitutive Modeling

The Abaqus FE program has been used to simulate the concrete, and the CDP model of concrete damaged plasticity has been used. Numerous researchers have utilized the CDP model to study the constitutive behavior of concrete [42,43]. The CDP model uses the following formulation in Equations (1) and (2) to characterize concrete's constitutive behavior under compression and tension.

$$ß_t = (1 - V_t){E_0}^{em} : (\varepsilon - {\varepsilon_t}^{em}) \quad (1)$$

$$ß_c = (1 - V_c){E_0}^{em} : (\varepsilon - {\varepsilon_c}^{em}) \quad (2)$$

The tensile and compressive stress vectors are indicated by $ß_t$ and $ß_c$, respectively. The ${\varepsilon_t}^{em}$ and ${\varepsilon_c}^{em}$ are the tensile and compressive plastic strain equivalents, respectively. The initial undamaged elastic modulus, denoted by ${E_0}^{em}$, has been calculated based on the strain and stress response of a uniaxial compressive strength test performed on concrete [44]. Plastic strains are the dependent variables in the damage equation [45]. Lubliner et al. [44] created the first version of the CDP model's yield function, which was later revised by Lee and Fenves [45]. The Abaqus/Explicit User's Manual [36] has information on the CDP

yield function. There is no associative flow in the CDP model. The eccentricity and the dilation angle control the plastic potential process, measured at the deviatoric stress plane.

$$C_f = 1.4\,(\frac{C_{fp} - 8}{10})^{2/3} \tag{3}$$

$$F_g = (0.0469\,{a_g}^2 - 0.5\,a_g + 26)\,(\frac{C_{fp}}{10})^{0.7} \tag{4}$$

Table 4 displays the technical characteristics of using the CDP model to model concrete. Carreira and Chu [46] proposed a method for generating the stress–strain response of concrete with a characteristic strength (C_{fp}) of 30 MPa. When the stresses in concrete reach a level greater than 0.3 C_{fp}, it is hypothesized that the material will begin to act elastically (when subjected to compression). When subjected to uniaxial stress, the fracture energy approach predicted the concrete's tensile behavior [9]. A linear softening model has been used to indicate the tensile failure of concrete. We used Equations (3) and (4) to figure out C_f, which stands for the tensile strength of the concrete, and F_g, which stands for the fracture energy. The concrete compressive strength (C_{fp}) and the maximum aggregate size (a_g) have been used in the process of determining the C_f and the G_f, respectively [36,42].

2.4. Mesh Sensitivity Analysis Model

Mesh sensitivity analyses were performed to investigate mesh size influence on the MSE wall's seismic response. Except for the steel reinforcement, the FE model was modeled using plane strain elements with reduced integration and hourglass control (CPE4R). A beam element (B31) was used to mesh the steel reinforcement (rebar) [35]. Numerous scholars have investigated the impact of mesh size on structural response and noted that the findings of finite element analysis exhibit a high degree of sensitivity to changes in mesh size. Additionally, it has been shown that selecting an optimal mesh size may lead to more precise finite element (FE) results while reducing computing time [16,20]. During the FE investigations conducted by Tiwari et al. [35], it was discovered that the backfill near the retaining wall stem and the heel slab have a significant impact on the seismic response of the earth-retaining wall. Consequently, mesh sensitivity assessments have been conducted to evaluate the effects of varying mesh sizes on the accuracy of the computational model at the points of contact between the mechanically stabilized earth (MSE) wall and the backfill material. The mesh sensitivity assessments were carried out by altering the mesh sizes of the stem and heel of the model. A medium-density mesh was used for the finite element analysis to reduce the shear-locking effects. The mesh sensitivity studies have used four different mesh sizes: 25 mm, 50 mm, 75 mm, and 100 mm. Mesh sensitivity analyses were conducted using the FE model. A minor distinction has been observed between the outcomes of various model mesh sizes. A 25 mm mesh size was chosen based on mesh sensitivity analyses for the comprehensive FE investigations [35].

2.5. Simplified Analytical Model

An FE study on MSE wall models estimates earthquake-induced displacement. FE investigations on full-scale MSE wall models need FE simulation and constitutive modeling competence. A force-based displacement check model has been proposed to estimate the maximal earthquake-induced elastic displacement (£max) of the MSE wall with granular backfill [22,31]. Figure 2 depicts the MSE wall considered during formulation development. The height and thickness of the model are respectively denoted by "h" and "w_t".

The body force at the wall's unit height $(M1_{CD})$ is determined.

$$W1_{AE} = HF_A \times C_k \times \omega_{wall} \tag{5}$$

Backfill dynamic pressure coefficient according to the Mononobe–Okabe method:

$$K_{AE} = \frac{cos^2\ (\varnothing - \theta - \alpha)}{cos\varphi cos^2\theta\ (\Delta + \theta + \alpha)\left[1 + \sqrt{\frac{sin(\Delta+\varnothing\ )sin(\varnothing-\gamma-\alpha)^2}{cos(\Delta+\theta+\alpha)cos(\gamma-\theta)}}\right]} \quad (6)$$

Dynamic soil pressure at the base of the MSE wall:

$$S_{AE} = HE_A K_{AE} \Delta_{backfill} h \quad (7)$$

The (S_{AE}) is used to represent a triangular load per MSE wall unit width.

$$(M2_{CD}) \quad (8)$$

The greatest possible movement caused by the inertia of the MSE wall is determined.

$$£1_{max} = \left(\frac{B1_{Fs}\ h4}{8EI}\right) \quad (9)$$

$$MSE\ Wall = (HF_A \times C_k \times \Omega_{wall}) \quad (10)$$

The maximum displacement caused by dynamic soil pressure is calculated.

$$£2_{max} = \left(\frac{B2_{Fs}\ h4}{30EI}\right) \quad (11)$$

The utmost elastic displacement exhibited by the MSE wall is determined.

$$£_{max} = £1_{max} - £2_{max} \quad (12)$$

Figure 4 depicts the seismic body force ($M1_{CD}$) on the MSE wall stem and the dynamic soil force per unit width of the walls ($M2_{CD}$) along the wall height (assuming a triangular distribution). The MSE wall supports a homogeneous, horizontal, granular backfill behind it, and it should be highlighted. The MSE wall and backfill contact angle (ø) have been considered, $ø/2$. The MO equation has been used to predict the seismic pressure behind the wall stem [31]. The pseudo-static pressure on the MSE wall stem is calculated using the MO equation, and it grows linearly with wall depth. The pseudo-static lateral pressure coefficient (S_{AE}) was calculated to be 100% S_h. Equation (6) calculates the seismic force (S_{AE}) along the MSE wall height, where A_{FH} is the backfill's horizontal acceleration amplification. The formulation utilized to determine the maximum displacement resulting from the retaining wall inertia forces ($£1_{max}$) has been computed as follows: the variables used in this context are E, representing Young's modulus of the retaining wall; I, describing the moment of inertia of the retaining wall; backfill, representing the unit weight of the backfill; k_h, representing the horizontal seismic coefficient; and W_{wall}, representing the weight of the retaining wall. The calculation of $(£2_{max})$, which represents the maximum displacement resulting from the seismic active pressure of backfill, has been determined utilizing the subsequent formulation:

The equation $(M2_{CD})$ = S_{AE} denotes the seismic force per unit width of the retaining wall. Upon computation of $£1_{max}$ and $£2_{max}$, the maximum displacement at the top of the retaining wall can be determined by submitting said values. The process for estimating the earthquake-induced elastic displacement of the base-restrained retaining wall with cohesionless backfill is illustrated in detail in Equations (5)–(12).

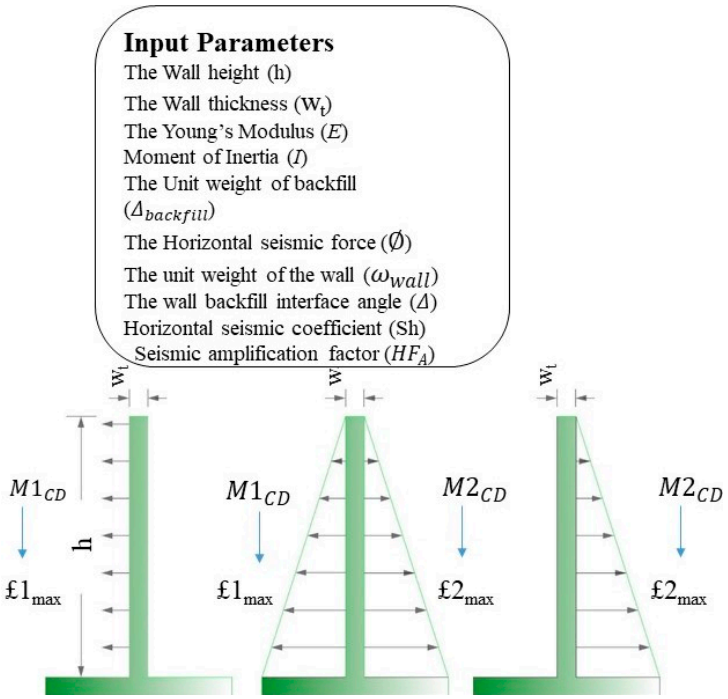


Figure 4. Input estimating MSE-retaining wall maximum elastic seismic displacement.

2.6. Validation of FE Modeling Approach

In this work, the authors conducted reinforcement concrete wall and precast concrete wall modeling to validate the capabilities of the current FE modeling technique. A 3D plane strain FEA model of the full-scale wall model has been created using the FEA modeling method. The backfill was modeled using the MC material model, and all wall-facing-panels models were modeled using the concrete damaged plasticity (CDP) [31,44]. Analyses of nonlinear time histories have been carried out with the help of the dynamic explicit scheme that the FE program Abaqus provides. It is important to note that the recorded displacement time history of the earthquake shaking base was utilized to construct the input base excitation for the FEA models. The results from FE simulations were found to correlate very well with those from the all-walls model. The seismic reactions of the prototype retaining walls connect rather well [31]. This indicates the current FE modeling technique can reproduce the seismic response of base-restrained retaining walls in a virtual environment in an accurate manner.

3. Seismic Input Excitations

This research explores the seismic behavior of mechanically stabilized earth (MSE) walls using a finite element analysis under earthquake conditions equivalent to those utilized in the analysis's base movements. Harmonic excitations of changing amplitudes but constant frequency were used as the basis for the model's initial movements [47]. The strength of these stimulations was gradually raised from low peak acceleration amplitudes for brief periods to high peak acceleration amplitudes for a specific time [48]. The earthquake occurred on 24 September 2019, at approximately 16:02 local time and had a focal depth of 10 km. The magnitude of this earthquake was estimated to be 6–6.5 on the Richter scale, with a peak ground acceleration of approximately 4 m/s^2, and the major frequency components were up to 15 Hz. Figure 5 depicts the time history of acceleration applied to the FE model for seismic evaluation, along with the frequency components of the time series (GSP, EERA [6,7]).

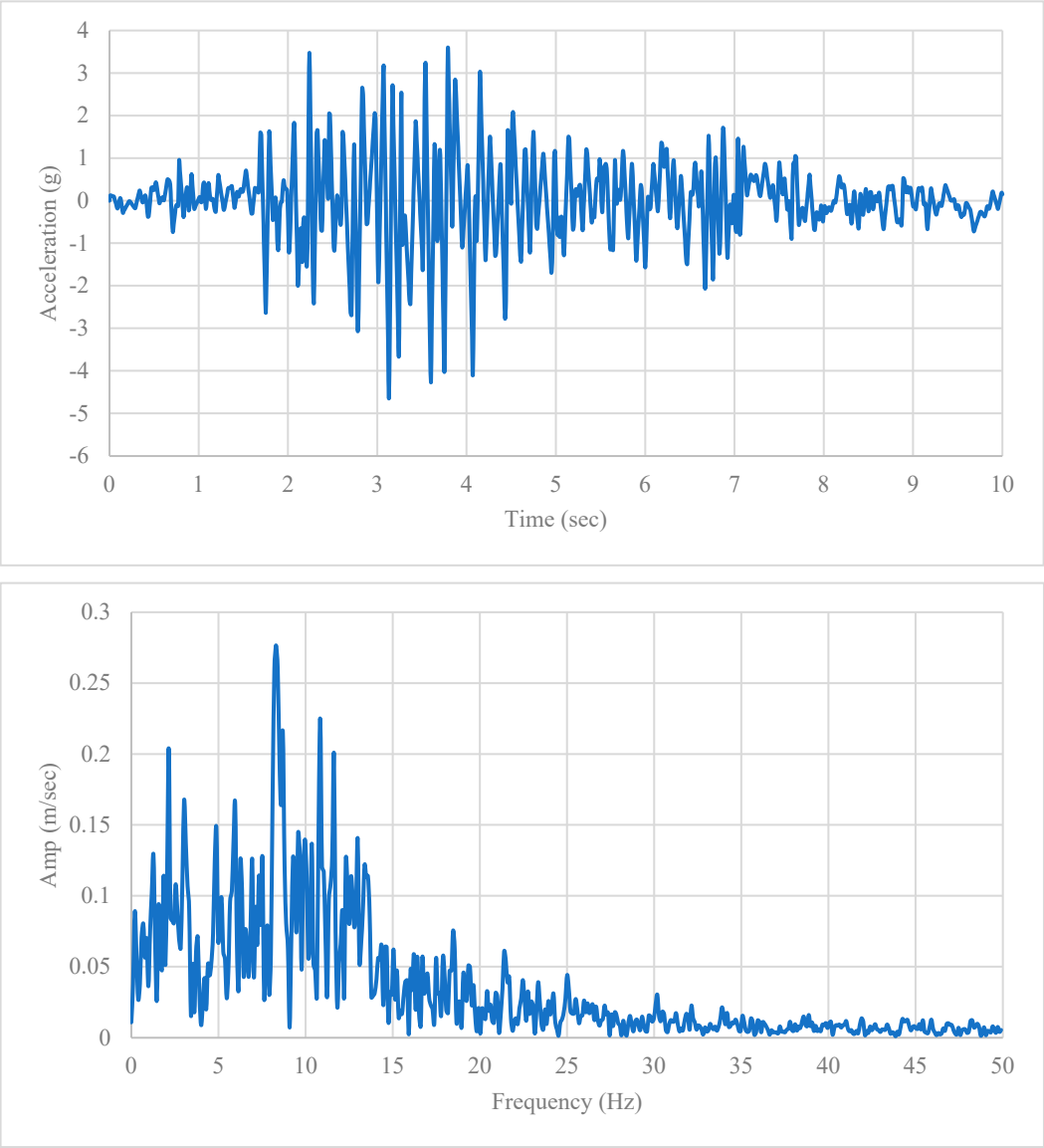


Figure 5. Earthquake N/S data (data source: Geological Survey of Pakistan [6]).

4. Results and Discussion

A thorough investigation of multiple variables was conducted for design and to compare the performance of hollow precast concrete MSE walls (PC1-W and PC2-W) exposed to ground excitation over time with a reinforcement concrete MSE wall (CR-W); extensive research has been conducted on numerous parameters. The input ground excitation exhibits a vertical and horizontal peak ground acceleration (PGA). The numerical simulation results of the PC-W1, PC-W2, and CR-W MSE walls, which are 6 m, 8 m, and 6 m tall, respectively, encompassed a wide range of results such as top displacement of the wall, vertical pressure of the wall, horizontal pressure of the wall, lateral pressure of the wall, settlement of the wall, settlement of the backfill geogrid, vertical pressure of the backfill, horizontal pressure of the backfill, lateral pressure of the backfill, vertical settlement of the foundation, and stress distribution of the wall. The following section outlines these results.

4.1. Top Displacement of Wall

A complete and rigorous FE analysis was conducted to understand the seismic response of these three kinds of MSE walls (PC-W1, PC-W2, and CR-W). The impact of varying wall heights on the seismic behavior of walls has been investigated by implement-

ing nonlinear time history finite element analysis, as stated in Section 3. Figure 6 shows the changes in the relative displacement at the top of the PC-W1, PC-W2, and CR-W walls over time when considering different base excitations and wall heights. Increasing peak ground acceleration (PGA) results in higher relative displacements at the upper wall height sections.

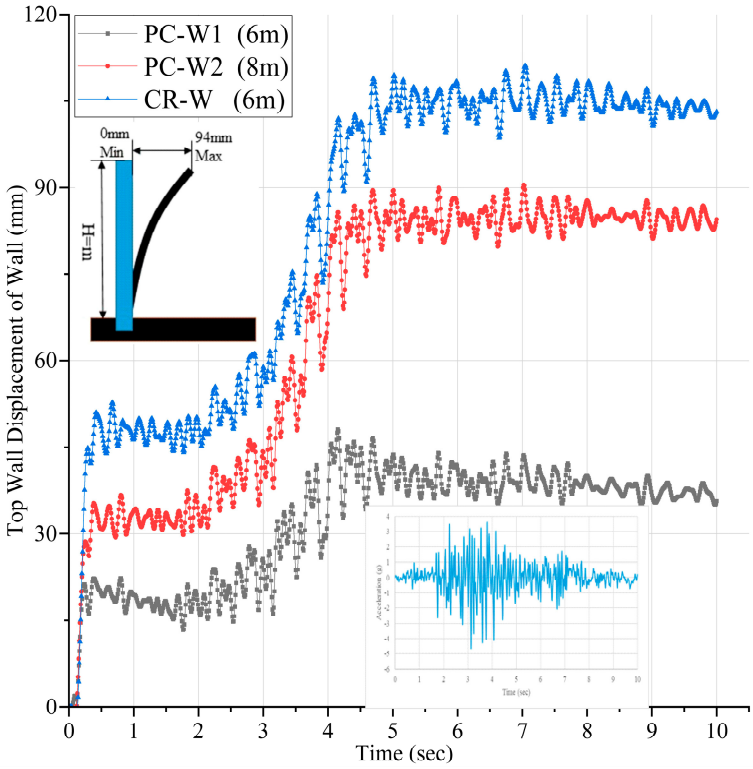


Figure 6. Top Displacement of Wall.

The finite element analysis findings also indicated that the relative displacement of the MSE walls is only observable in the "x" direction, which is away from the backfill and corresponds to the active state. This displacement is primarily caused by the significant inertial forces exerted by the backfill. The shaking table studies revealed a comparable active displacement of the retaining wall [35]. The results of the FE analysis also showed that, due to the backfill's high inertial forces, the relative displacement of the MSE walls occurs only in the "x" direction (i.e., away from the backfill active state). The findings demonstrate that the PC-W2 and CR-W walls exhibit greater displacement when stimulated with synthetic accelerograms. Due to the higher amplifications of horizontal accelerations in the backfill, high inertial forces are applied to the MSE walls, resulting in a more significant seismic displacement of the facing wall panels with the backfill. However, when agitated with historical accelerograms, the MSE wall with different heights displays almost separate displacements. This showed that the PC-W1 structural design is more reliable than the PC-W2 and CR-W walls. When the historical accelerogram with 0.5 s > 1.5 g is applied to the MSE wall, all three wall types show almost the same relative movement. At the end of the 0.4 g accelerogram for 10 s, the PC-W2 and CR-W displacement is higher than for PC-W1.

4.2. Backfill Earth Pressure

The lateral pressures exerted by the backfill along the orthogonal direction are shown in Figure 7A, according to FE analysis of the response of walls (i.e., PC-W1, PC-W2, and CR-W) under earthquake loading. In most cases, the vertical ground acceleration has improved the backfill's confining pressure and soil stiffness. However, the study found that the PC-W2 and CR-W lateral pressure compression was slightly higher, which aligns

with the findings of Munoz H et al. [26,27]. Figure 7A demonstrates that lateral backfill pressure increases with depth, reaching a maximum near the foundation. This means that the strength and stiffness of the reinforcing layers should be chosen carefully to handle the pressure rise and that the design of walls should consider the fluctuation of lateral pressure with depth. Results from PC-W1 indicate that the behavior of the backfill lateral earth pressure is low compared to PC-W2 and CR-W.

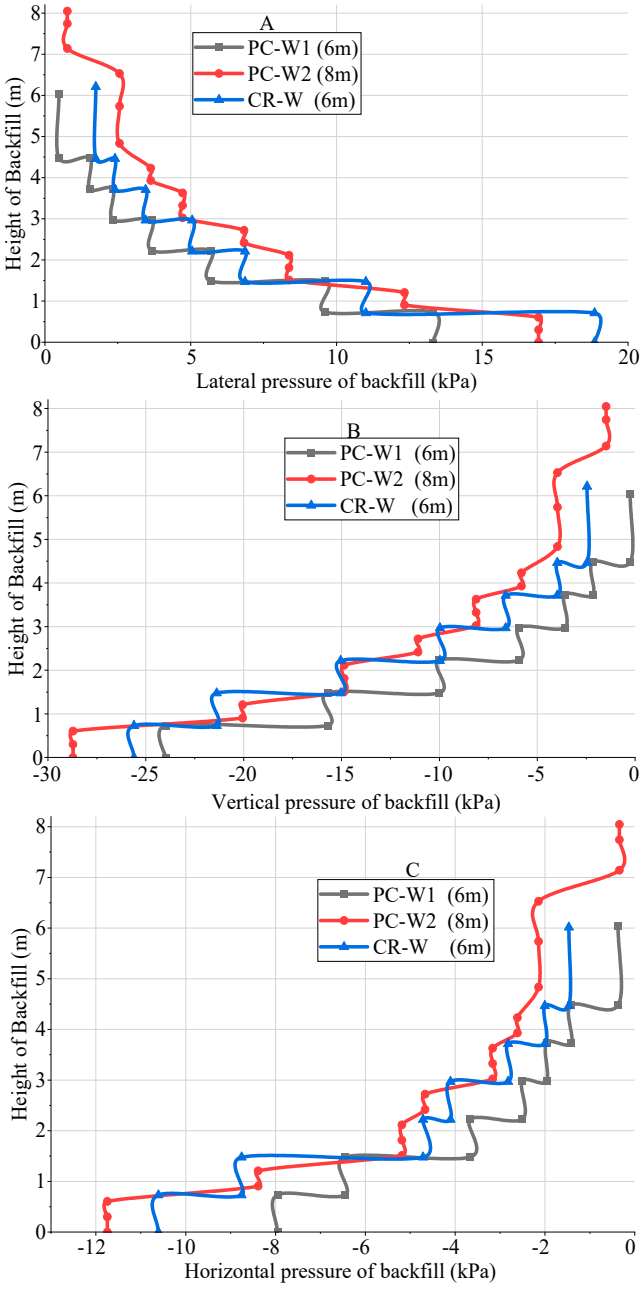


Figure 7. Backfill earth pressures at the back; (**A**) lateral earth pressure; (**B**) vertical earth pressure; (**C**) horizontal earth pressure.

Figure 7B illustrates maximum vertical earth pressure distributions at the base excitations. The shaking levels in the results show different trends for all MSE walls and vertical backfill pressure, with the vertical pressures being mostly uniform across most of the backfill width but increasing significantly with backfill height. The highest vertical backfill pressure values are similar to those reported in earlier investigations [5,31]. Figure 7B shows the vertical earth pressures acting at the back of the backfill from top to bottom at

the layers of the soil of the reinforcement backfill in all cases (PC-W1, PC-W2, and CR-W). The PC-W2 and CR-W backfill vertical pressure gradually increased, as observed in the height at the backfill layers. At the top of the reinforcement backfills, the vertical pressure pressures are lower than those just below. This is because the horizontal fill displacements in these locations were larger in the CR-W and PC-W2 walls than in the PC-W1 wall.

The distribution of horizontal earth pressure over the height of the backfill (PC-W1, PC-W2, and CR-W) of the MSE walls is presented in Figure 7C. The FE analysis results indicate that the incremental active horizontal earth pressures were predominantly negative, especially in the lower portion of the wall. The sharp PC-W2 and CR-W backfill jumps can be observed in the pressure against the height of backfill. Just above the top of the reinforcement backfill, these pressures are lower than those just below. These findings are supported by studies demonstrating reduced active horizontal earth pressure to values under seismic loadings, such as the numerical simulation highlighted in [5] and models and tests [31,32]. The behavior of PC-W1 is consistent with the lower horizontal earth pressures depicted in Figure 7C at the same location. PC-W1 results demonstrate that the backfill's horizontal earth pressure behavior is better than those of PC-W2 and CR-W. This is because the horizontal fill displacements in these locations were larger in the CR-W and PC-W2 walls than in the PC-W1 walls.

4.3. Earth Pressure of Wall

The measured distributions of lateral wall pressure across wall height at particular peak base acceleration amplitudes are shown in Figure 8A, including the lateral wall pressure across the wall height for a given peak base acceleration. The results indicate that the total active lateral wall pressures oscillated the positive values between the top and bottom of the wall, gradually approaching zero towards the top. The impact of lateral pressure on the mid-section of the wall is high, as shown in Figure 8A. The findings demonstrated that the lateral pressure of the mid-section of PC-W1 is low compared to PC-W2 and CR-W walls. During the initial stages of the seismic event, the lateral pressure exhibits significant fluctuations for 10 s. However, beyond this point, the lateral pressure steadily increases with minimal variation in magnitude for the 8 m and 6 m tall MSE-retaining walls. This is attributed to the lower lateral pressure exerted by PC-W1 compared to CR-W and PC-W2 walls, making them more effective in their lateral wall pressure. When designing wall structures, consideration is given to both horizontal and vertical vibrations. The acceleration at a specific depth (x), accounting for horizontal and vertical movements in the wall, can be expressed using Equations (12) and (13) proposed by [23].

$$\mathrm{m}_{(\mathrm{yu})}(\mathrm{x},\mathrm{T}) = [1 + \frac{h-x}{h}\ (Gf-1)]\ \mathrm{m}_{(\mathrm{yu})}\ \mathrm{Sin\ w}\ (\mathrm{T} - \frac{(h-x)}{Uvv}) \tag{13}$$

$$\mathrm{b}_{(\mathrm{sv})}(\mathrm{x},\mathrm{T}) = [1 + \frac{h-x}{h}\ (Gf-1)]\ \mathrm{b}_{(\mathrm{sv})}\ \mathrm{Sin\ w}\ (\mathrm{T} - \frac{(h-x)}{Usp}) \tag{14}$$

Figure 8B shows the distribution of the vertical earth pressures of the three wall elevations (PC-W1 6 m, PC-W2 8 m, and CR-W 6 m) for the 4 m reinforcement backfill. The calculated vertical earth pressure is compared with the three MSE wall models as follows: the findings show that the calculated vertical earth pressures were high up to the mid height for both PC-W2 and CR-W at different elevations. There is a location-related increase for the vertical earth pressure at a distance of 3.0 m from the bottom of the facing. This phenomenon is because the interface shear transfer and the local arching develop between the soil and the wall facing, which resulted in down-drag forces on the facing. A similar pattern of increasing vertical earth pressure behind the facing has been reported for walls embedded in a foundation [14,15]. The present study assesses the effects of base excitations by contrasting our findings with those of Bakr J and Ahmad SM; according to the conclusions of [9], seismic accelerations are predominantly enhanced by vertical excitations towards the top of the soil zones, highlighting that the vertical excitation

influences wave propagation. The change in pressure from positive to negative is attributed to the wall's height.

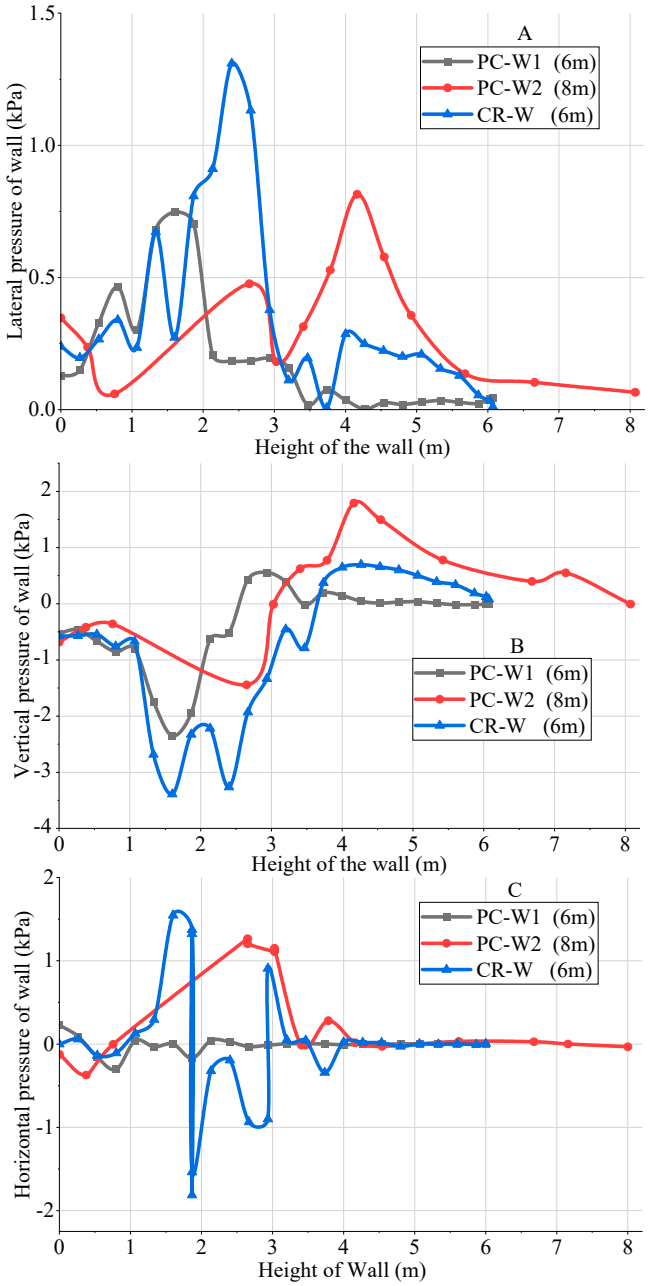


Figure 8. Earth Pressure of Wall; (**A**) lateral earth pressure of wall; (**B**) vertical earth pressure of wall; (**C**) horizontal earth pressure of the wall.

The distribution of horizontal wall pressure over the height of hollow precast walls (PC-W1, PC-W2) and reinforcement concrete walls (CR-W) is shown in Figure 8C. The finite element analysis of the MSE wall's seismic response reveals some interesting results. Figure 8C shows the distribution of the horizontal earth pressures at three wall elevations (6.0, 8.0, and 6.0 m). The magnitude and distribution of horizontal earth pressures for the PC-W1 wall were different from those for the CR-W and PC-W2 walls except for the locations of the wall facing, where the horizontal earth pressure for the PC-W1 wall was lower than that for the CR-W and PC-W2 walls. This is because the horizontal fill displacements in these locations were larger in the CR-W and PC-W2 walls than in the PC-W1 wall. Large horizontal displacement indicated the fill approached the active earth

pressure state, thereby reducing the horizontal earth pressure in the wall. The findings show that the horizontal earth pressure is higher at the bottom and mid-section of the wall facing and lower at the top of the wall facing. The PC-W1 wall significantly reduces the horizontal earth pressures.

4.4. Vertical Settlement of Foundation

Figure 9 illustrates the calculated vertical settlement of the foundation and the vertical pressure the facing wall panel exerts on the base case footing. The middle of the wall, right below the centerline of the foundation, is where the data with solid symbols are from. The data points with open symbols show that the toe load pressures differ throughout the wall's running length. A two-dimensional model cannot identify this small three-dimensional impact. Because the distributions of foundation vertical settlement at the same three places were not practically discernible, they were not depicted to prevent visual clutter. The vertical toe pressure exceeds the pressure resulting from the panels' self-weight (the footing load factor) owing to a down-drag on both the rear of the MSE wall panels and the foundation. This suggests that wall height and depth below the foundation influence the foundation's vertical settlement. The PC-W2 wall height is different from those of the PC-W1, CR-W analyzed walls, and the vertical settlement is slightly larger than those of the other two walls analyzed. A slight increase in the height of the wall affects the foundation settlement considerably due to the overturning moment generated by the lateral pressure developed from the backfill.

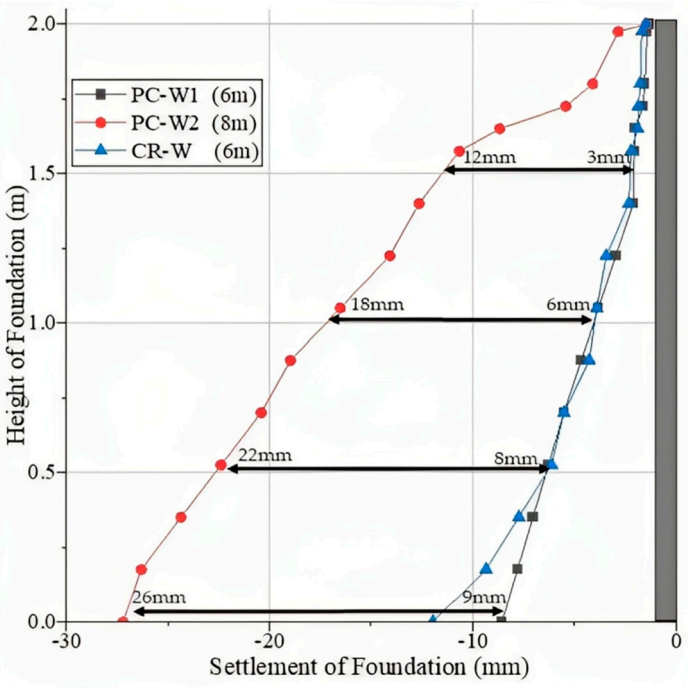


Figure 9. Vertical Foundation Pressure.

The vertical settlement of the foundation progressively changes; the vertical settlement is larger at various spots throughout the wall's running length. Figure 7 shows that the vertical settlement at the same positions on the wall is now 8 mm, 30 mm, and 13 mm for PC-W1, PC-W2, and CR-W, respectively. Finally, the findings show that the vertical settlement of the PC-W1 wall foundation is meager due to the wall's self-weight compared to the other walls. PC-W2, CR-W, and the calculated vertical settlement in Figure 9 are typical of observed values for field walls reported in the literature [19]. In the AASHTO, the suggested range for the design of bearing pads for incremental concrete panel walls is 20–30 mm [3,49].

4.5. Vertical Settlement of Wall

Under base excitation, simulated data show the observed time history of PC-W1, PC-W2, and CR-W wall settlement. Figure 10 demonstrates that the wall can absorb shocks and maintain a uniform height unless the base is lowered to a specific depth. The stability in settlement can be observed after half of the excitation. Settlements of the wall increase over time and distance from the face and are more extensive in flexible base materials. The wall settlement (PC-W1, PC-W2, and CR-W) is about 22 mm, 35 mm, and 31 mm, respectively. Figure 8 shows that the lowest settlements for each wall case in each plot are near the connections, which is consistent with the wall drooping over the foundation, as previously indicated [22]. The results show that the PC-W1 wall was significantly resistant to settling under seismic forces due to its lightweight and high structural resilience resistance. On the other hand, the PC-W2 and CR-W walls have higher vertical settlement when subjected to seismic forces.

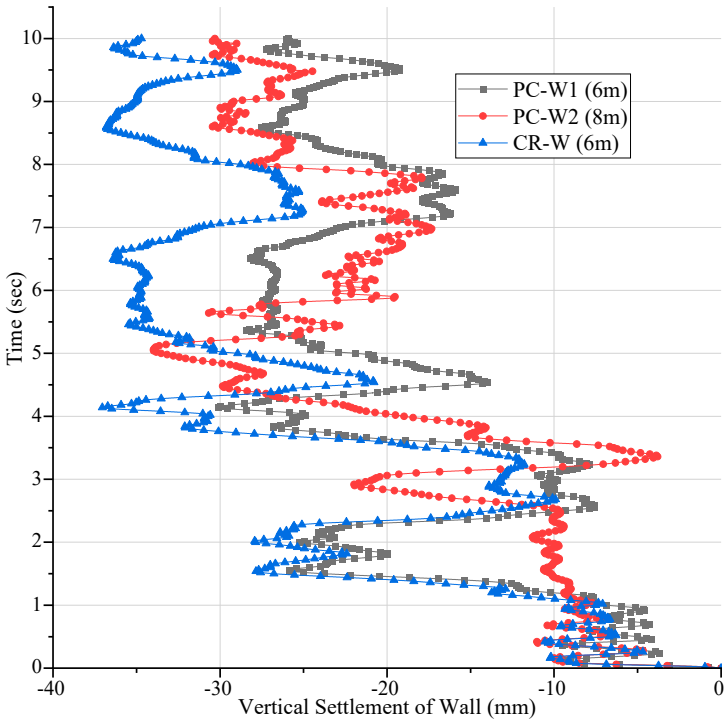


Figure 10. Settlement of the Wall.

The (PC-W1, PC-W2, and CR-W) settlement increased with time, with a minor settlement at the bottom and a maximum settlement towards the top. This indicates that the seismic motion's input time significantly impacts the wall's settlement. However, the settlement distribution behavior of the PC-W1 wall differed from that of the PC-W2 and CR-W walls. After a seismic acceleration time of 4.5 s, the settlements in the MSE wall became consistent, as shown in Figure 10. In the AASHTO, the suggested range for the design of bearing pads for incremental concrete panel walls is 40–50 mm [3,49].

4.6. Vertical Settlement of Geogrid Backfill

The Figure 11 inset shows that the geogrid backfill settlement behind the PC-W1, PC-W2, and CR-W MSE walls. The incremental settlement of the backfill behind the wall has been observed, and it is found that under the influence of seismic excitation, the backfill reinforcement has a similar time history of settlement trend with the increasing order of PC-W1, PC-W2, and CR-W. It has been determined that when subjected to seismic excitation, the reinforcement backfill experiences settlement patterns that closely resemble the increasing order of settlement seen in the PC-W1, PC-W2, and CR-W walls. Figure 11 depicts vertical settlement profiles for geogrid-supported backfill layers. The datum for these plots is

the wall toe elevation at the beginning of the wall construction. Geogrid backfill could effectively reduce seismic settlements of backfill surfaces and provide seismic settlement resistance for the reinforced MSE wall. The maximum settlement of geogrid backfill (PC-W1, PC-W2, and CR-W) is approximately 8 mm, 12 mm, and 20 mm, respectively. The above findings demonstrate that for each wall case in each plot, the minimum settlements are close to the connections, which is consistent with the soil drooping over the reinforcement as previously described [5,32]. The findings indicate that the PC-W1 and CR-W geogrid backfill exhibited significant resistance to settling under seismic conditions.

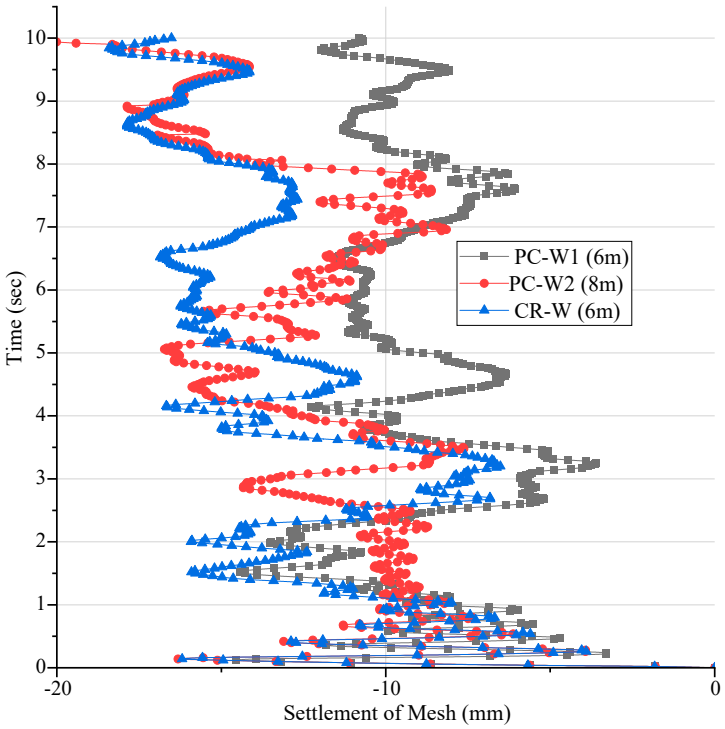


Figure 11. Settlement of the Backfill Reinforcement.

4.7. Stress Distribution of Wall

The stress distributions along the height of different MSE walls (PC-W1, PC-W2, and CR-W) were examined. Figure 12 displays the stress distribution, indicating that the maximum stress was observed at the bottom while the minimum stress was found at the top. In contrast, a gradual increase in stress was observed along the bottom arm of the wall. Figure 12 reveals a gradual increase in stress against the wall's arm, while it was found that the upper arm flexed the most. The above findings demonstrate that as the height of the wall increased, the stress decreased, with the highest stress occurring at the bottom. To validate the consistency of our results and contribute to the existing body of knowledge, we compared our findings with those of previous researchers who have investigated stress distribution behavior in concrete retaining walls under seismic loading conditions. For instance, the authors of [28,29] conducted studies on the dynamic response of concrete retaining walls, including stress distribution analysis. Their research emphasized the importance of accurate prediction and control of stress distribution to ensure the stability and performance of concrete retaining walls under seismic forces. The stress distributions in MSE walls rise to the wall height. This shows that the upper area of the walls experiences the lowest stress. However, the stress distribution behavior in the PC-W1 wall differed from that of PC-W2 and reinforcement concrete (CR-W) walls. The wall stress distributions (PC-W1, PC-W2, and CR-W) are about 22 MPa, 10.3 MPa, and 7.5 MPa, respectively.

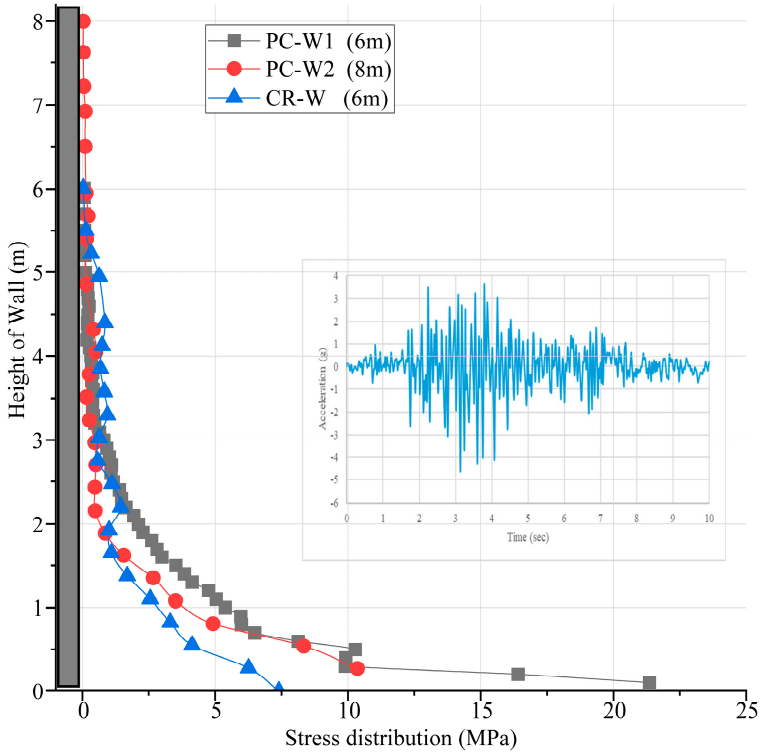


Figure 12. Stress distribution of retaining wall.

5. Conclusions, Policy Recommendations, and Future Research Direction

5.1. Conclusions

A parametric analysis examined the seismic response characteristics of a mechanically stabilized earth (MSE) wall with geogrid-reinforced granular backfill. Top displacement of the wall, vertical pressure of the wall, horizontal pressure of the wall, lateral pressure of the wall, settlement of the wall, settlement of the backfill geogrid, vertical pressure of the backfill, horizontal pressure of the backfill, lateral pressure of the backfill, vertical settlement of the foundation, and stress distribution of the wall were compared in detail under seismic ground motions, This research compared the worldwide performance of reinforcement and prefabricated (MSE) walls under identical environmental and seismic conditions. The following conclusions could be drawn:

- The stress level on the bottom of the valve stem in PC-W1 has been found to be decreased by about 40%, and the displacement has been reduced by 50–60%. Owing to the reduction in stress and deflection level, it is concluded that PC-W1 is significantly more stable than CR-W and PC-W2 MSE walls in terms of seismic response. The stress distribution in CR-W and PC-W2 MSE walls declined with rising wall height, while the displacement was increased with the height and maximum displacement at the top.
- The study reveals a notable decrease of approximately 21% in the magnitude of lateral pressure exerted on the valve stem within the hollow prefabricated MSE wall. A significant reduction in wall settlements, ranging from 15% to 20%, has also been observed. It is concluded that prefabricated MSE walls are significantly more stable than reinforced concrete walls regarding seismic response. The settlement of MSE walls increased as the wall height increased. In contrast, the settlement of the wall demonstrated an increase in proportion to its height, reaching its maximum at the uppermost section.
- The settlements of the backfill surface depended on the height of the backfill. The geogrid could effectively decrease seismic settlement of the backfill surfaces. The backfill surface settlement in the PC-W1 and CR-W reinforced zone was much smaller

than in PC-W2. The geogrid provided seismic settlement resistance ability for the reinforced MSE walls. The above research results could provide references for the seismic design and construction of MSE walls with geogrid backfill.

5.2. Policy Recommendations and Future Research Direction

- With a 15% reduction in bottom bar thickness and a 20% reduction in precast wall volume, the new design is more cost-effective and environmentally friendly. In terms of environmental efficiency, the precast concrete MSE wall outperformed the reinforcement concrete (MSE) retaining wall. The comparative study found that the prefabricated concrete (MSE) walls performed better than reinforcement concrete MSE walls in highly seismic areas, including carbon dioxide (CO_2) emissions, greenhouse gas (GHG) effects, essential material expenditure, and embodied energy.
- Considering the effects of the height of the MSE wall and the acceleration level of the seismic input motion, unique design schematics were created to illustrate the relationship between the seismic earth pressure and the movement of the MSE wall. The MSE walls are considered thick and nonbending from a geotechnical engineering viewpoint. Hence, they can resist the seismic passive earth pressure force development when moving toward the backfill soil. However, this circumstance is crucial for the stability of embedded MSE walls and the structural design of MSE wall types. Additional research is necessary to comprehensively understand these critical geotechnical structures' seismic resilience.

Author Contributions: Conceptualization, M.A.; methodology, M.A.; software, M.A.; validation, M.A. and G.N.; formal analysis, M.A.; investigation, M.A.; resources, H.P. and G.O.; data curation, M.A.; writing—original draft preparation, M.A.; writing—review and editing, G.N. and B.A.; visualization, G.O.; supervision, H.P.; project administration, H.P. All authors have read and agreed to the published version of the manuscript.

Funding: This work was supported by Second Tibetan Plateau Scientific Expedition and Research Program (Grant No. 2019QZKK0902), the Science and Technology Research Program of Institute of Mountain Hazards and Environment, CAS (IMHE-ZDRW-01), and the National Natural Science Foundation of China, China (Grant numbers: 42077275 & 42271086).

Data Availability Statement: The datasets analyzed during the current study are not publicly available as they are still being used for subsequent research but are available from the corresponding author on reasonable request.

Acknowledgments: The authors would like to acknowledge the Institute of Mountain Hazards Environment, Chinese Academy of Sciences, Chengdu, China for providing us the platform to conduct this valuable research.

Conflicts of Interest: The authors declare no conflict of interest.

References

1. Abdelouhab, A.; Dias, D.; Freitag, N. Numerical analysis of the behavior of mechanically stabilized earth walls reinforced with different types of strips. *Geotext. Geomembr.* **2011**, *29*, 116–129. [CrossRef]
2. Allen, T.M.; Bathurst, R.J. Geosynthetic reinforcement stiffness characterization for MSE wall design. *Geosynth. Int.* **2019**, *26*, 592–610. [CrossRef]
3. AASHTO. *AASHTO LRFD Bridge Design Specifications*, 9th ed.; American Association of State Highway and Transportation Officials: Washington, DC, USA, 2020.
4. AFNOR (Association Française de Normalisation). *Geotechnical Design Retaining Structures Reinforced and Soil Nailing Structures*; NFP 94-270; AFNOR: Paris, France, 2009.
5. Damians, I.P.; Bathurst, R.J.; Olivella, S.; Lloret, A.; Josa, A. 3D modelling of strip reinforced MSE walls. *Acta Geotech.* **2020**, *16*, 711–730. [CrossRef]
6. Geological Survey of Pakistan (GSP). 2022. Available online: https://gsp.gov.pk/ (accessed on 10 September 2021).
7. Earthquake Reconstruction & Rehabilitation Authority (ERRA). 2022. Available online: http://www.erra.gov.pk/ (accessed on 10 September 2021).

8. Bathurst, R.J.; Miyata, Y.; Allen, T.M. Deterministic and probabilistic assessment of margins of safety for internal stability of as-built PET strap reinforced soil walls. *Geotext. Geomembr.* **2020**, *48*, 780–792. [CrossRef]
9. Bakr, J.; Ahmad, S.M. A finite element performance-based approach to correlate movement of a rigid retaining wall with seismic earth pressure. *Soil. Dyn. Earthq. Eng.* **2018**, *114*, 460–479. [CrossRef]
10. Bourgeois, E.; Soyez, L.; Le Kouby, A. Experimental and Numerical study of the behavior of a reinforced-earth wall subjected to a local load. *Comput. Geotech.* **2011**, *38*, 515–525. [CrossRef]
11. Cai, Z.; Bathurst, R.J. Seismic response analysis of geosynthetic reinforced soil segmental retaining walls by finite element method. *Comput. Geotech.* **1995**, *17*, 523–546. [CrossRef]
12. Capilleri, P.P.; Ferraiolo, F.; Motta, E.; Scotto, M.; Todaro, M. Static and dynamic analysis of two mechanically stabilized earth walls. *Geosynth. Int.* **2019**, *26*, 26–41. [CrossRef]
13. Cristelo, N.; Fe'lix, C.; Lopes, M.L.; Dias, M. Monitoring and numerical modelling of an instrumented mechanically stabilized earth wall. *Geosynth. Int.* **2016**, *23*, 48–61. [CrossRef]
14. Damians, I.P.; Bathurst, R.J.; Josa, A.; Lloret, A. Numerical analysis of an instrumented steel reinforced soil wall. *ASCE Int. J. Geomech.* **2015**, *15*, 4014037. [CrossRef]
15. Damians, I.P.; Bathurst, R.J.; Josa, A.; Lloret, A. Vertical facing panel-joint gap analysis for steel-reinforced soil walls. *ASCE Int. J. Geomech.* **2016**, *16*, 4015103. [CrossRef]
16. Cakir, T. Evaluation of the effect of earthquake frequency content on seismic behavior of cantilever retaining wall including soil–structure interaction. *Soil. Dyn. Earthq. Eng.* **2013**, *45*, 96–111. [CrossRef]
17. Daheur, E.G.; Goual, I.; Taibi, S.; Mitiche-Kettab, R. Effect of dune sand incorporation on the physical and mechanical behavior of tuff: (experimental investigation). *Geotech. Geol. Eng.* **2019**, *37*, 1687–1701. [CrossRef]
18. Ertugrul, O.L.; Trandafir, A.C. Seismic earth pressures on flexible cantilever retaining walls with deformable inclusions. *J. Rock. Mech. Geotech. Eng.* **2014**, *6*, 417–427. [CrossRef]
19. Keykhosropour, L.; Lemnitzer, A. Experimental studies of seismic soil pressures on vertical flexible, underground structures and analytical comparisons. *Soil. Dyn. Earthq. Eng.* **2019**, *118*, 166–178. [CrossRef]
20. Kuhlemeyer, R.L.; Lysmer, J. Finite element method accuracy for wave propagation problems. *J. Soil Mech. Found. Div.* **1973**, *99*, 421–427. [CrossRef]
21. Ling, H.I.; Liu, H.; Mohri, Y. Parametric studies on the behavior of reinforced soil retaining walls under earthquake loading. *J. Eng. Mech.* **2005**, *131*, 1056–1065. [CrossRef]
22. Nimbalkar, S.; Choudhury, D. Sliding Stability and Seismic Design of Retaining Wall by Pseudo-Dynamic Method for Passive Case. *Soil Dyn. Earthq. Eng.* **2007**, *27*, 497–505. [CrossRef]
23. Osouli, A.; Zamiran, S. The effect of backfill cohesion on seismic response of cantilever retaining walls using fully dynamic analysis. *Comput. Geotech.* **2017**, *89*, 143–152. [CrossRef]
24. Yazdandoust, M. Investigation on the seismic performance of steel-strip reinforced-soil retaining walls using shaking table test. *Soil. Dyn. Earthq. Eng.* **2017**, *97*, 216–232. [CrossRef]
25. Hokelekli, E.; Yilmaz, B.N. Effect of Cohesive Contact of backfill with Arch and Spandrel Walls of a Historical Masonry Arch Bridge on Seismic Response. *Period. Polytech. Civ. Eng.* **2019**, *63*, 926–937. [CrossRef]
26. Munoz, H.; Kiyota, T. Deformation and localization behaviours of reinforced gravelly backfill using shaking table tests. *J. Rock. Mech. Geotech. Eng.* **2020**, *12*, 102–111. [CrossRef]
27. Munoz, H.; Tatsuoka, F.; Hirakawa, D.; Nishikiori, H.; Soma, R.; Tateyama, M.; Watanabe, K. Dynamic stability of geosynthetic-reinforced soil integral bridge. *Geosynth. Int.* **2012**, *19*, 11–38. [CrossRef]
28. Tiwary, A.K.; Bhatia, S.; Singh, S.; Chohan, J.S.; Kumar, R.; Sharma, S.; Chattopadhyaya, S.; Rajkumar, S. Performance Comparison and Critical Finite Element Based Experimental Analysis of Various Forms of Reinforcement Retaining Structural System. *Math. Probl. Eng.* **2022**, *2022*, 4434679. [CrossRef]
29. Vlcek, J. Internal stability analyses of geosynthetic reinforced retaining walls. *Procedia Eng.* **2014**, *91*, 346–351. [CrossRef]
30. Nematollahi, B.; Voo, Y.L.; Sanjayan, J. Design and construction of a precast ultra-high performance concrete cantilever retaining wall. In Proceedings of the First International Interactive Symposium on UHPC-2016, Des Moines, IA, USA, 18–20 July 2016.
31. Tiwari, R.; Lam, N. Displacement based seismic assessment of base restrained retaining walls. *Acta Geotech.* **2022**, *17*, 3675–3694. [CrossRef]
32. Wang, L.; Chen, G.; Chen, S. Experimental study on seismic response of geogrid reinforced rigid retaining walls with saturated backfill sand. *Geotext. Geomembr.* **2015**, *43*, 35–45. [CrossRef]
33. Yoo, C.; Kim, S.B. Performance of a two-tier geosynthetic reinforced segmental retaining wall under a surcharge load: Fullscale load test and 3D finite element analysis. *Geotext. Geomembr.* **2008**, *26*, 460–472. [CrossRef]
34. Yu, Y.; Bathurst, R.J.; Miyata, Y. Numerical analysis of a mechanically stabilized earth wall reinforced with steel strips. *Soils Found.* **2015**, *55*, 536–547. [CrossRef]
35. Tiwari, R.; Lam, N. Modelling of seismic actions in earth retaining walls and comparison with shaker table experiment. *Soil. Dyn. Earthq. Eng.* **2021**, *150*, 106939. [CrossRef]
36. *Abaqus/Explicit User's Manual*, version 6.13; Dassault Systémes Simulia Corporation: Providence, RI, USA, 2013.
37. Dano, C.; Hicher, P.Y.; Tailliez, S. Engineering properties of grouted sands. *J. Geotech. Geoenviron. Eng.* **2004**, *130*, 328–338. [CrossRef]

38. Nadeem, M.; Akbar, M.; Pan, H.; Ou, G.; Amin, A. Investigation of the settlement prediction in soft soil by Richards Model: Based on a linear least squares-iteration method. *Arch. Civ. Eng.* **2021**, *67*, 491–506. [CrossRef]
39. Potts, D.M.; Zdravković, L. *Finite Element Analysis in Geotechnical Engineering: Theory*; Thomas Telford: London, UK, 1999.
40. Song, A. *Deformation Analysis of Sand Specimens Using 3D Digital Image Correlation for the Calibration of an Elasto-Plastic Model Dissertation*; Texas A & M University: College Station, TX, USA, 2012.
41. Yu, Y.; Bathurst, R.J.; Allen, T.M.; Nelson, R. Physical and numerical modelling of a geogrid reinforced incremental concrete panel retaining wall. *Can. Geotech. J.* **2016**, *53*, 1883–1901. [CrossRef]
42. Lima, M.M.; Doh, J.H.; Hadi, M.N.; Miller, D. The effects of CFRP orientation on the strengthening of reinforced concrete structures. *Struct. Des. Tall Spec. Build.* **2016**, *25*, 759–784. [CrossRef]
43. Tiwari, R.; Chakraborty, T.; Matsagar, V. Dynamic analysis of tunnel in weathered rock subjected to internal blast loading. *Rock. Mech. Rock. Eng.* **2016**, *49*, 4441–4458. [CrossRef]
44. Lubliner, J.; Oliver, J.; Oller, S.; Oñate, E. A plastic-damage model for concrete. *Int. J. Solids Struct.* **1989**, *25*, 299–326. [CrossRef]
45. Lee, J.; Fenves, G.L. Plastic-damage model for cyclic loading of concrete structures. *J. Eng. Mech.* **1998**, *124*, 892–900. [CrossRef]
46. Carreira, D.J.; Chu, K.H. Stress-strain relationship for plain concrete in compression. *J. Proc.* **1985**, *82*, 797–804.
47. Xu, J.-G.; Cao, X.-Y.; Shi, J.; Wang, Z. A comparative study of the novel externally-attached precast SRC braced-frames for seismic retrofitting under near-field spectrum-compatible non-stationary stochastic earthquake. *Structures* **2023**, *50*, 200–214. [CrossRef]
48. Feng, D.-C.; Wang, Z.; Cao, X.-Y.; Wu, G. Damage mechanics-based modeling approaches for cyclic analysis of precast concrete structures: A comparative study. *Int. J. Damage Mech.* **2020**, *29*, 965–987. [CrossRef]
49. FHWA. *Design of Mechanically Stabilized Earth Walls and Reinforced Slopes*; No. FHWA-NHI-10-024 Volume I and NHI-10-025 Volume II; Berg, R.R., Christopher, B.R., Samtani, N.C., Eds.; Federal Highway Administration: Washington, DC, USA, 2009.

Disclaimer/Publisher's Note: The statements, opinions and data contained in all publications are solely those of the individual author(s) and contributor(s) and not of MDPI and/or the editor(s). MDPI and/or the editor(s) disclaim responsibility for any injury to people or property resulting from any ideas, methods, instructions or products referred to in the content.